Inorganic Chemistry

pubs.acs.org/IC

Article

Experimental Testing of the Theoretically Predicted Magnetic Properties for Kagomé Compounds in the Li−Fe−Ge System

Aishwarya Mantravadi, Raquel A. Ribeiro, Sergey L. Bud'ko, Paul C. Canfield, and Julia V. Zaikina*

Cite This: *Inorg. Chem.* 2024, 63, 24697−24708

Read Online

ACCESS | Metrics & More | Article Recommendations | Supporting Information

ABSTRACT: Investigating material properties is essential to assessing their application potential. While computational methods allow for a fast prediction of the material structure and properties, experimental validation is essential to determining the ultimate material potential. Herein, we report the synthesis and experimental magnetic properties of three previously reported Kagome compounds in the Li−Fe−Ge system. $LiFe_6Ge_4$, $LiFe_6Ge_5$, and $LiFe_6Ge_6$ were predicted to have ferromagnetic or antiferromagnetic ground states. The hydride route that replaces the ductile Li metal with salt-like LiH proved to be an excellent alternative for the facile synthesis of the Li−Fe−Ge powders with appreciable purity, permitting the investigation of their bulk magnetic properties. Magnetometry below room temperature and room-temperature ^{57}Fe Mössbauer spectroscopy collectively indicate an antiferromagnetic ground state for the three compounds with ordering temperatures above 300 K, contrary to the prediction of ferromagnetic ground states. Moreover, Mössbauer spectroscopy reveals a magnetization of 1.1−1.3 μ_B/Fe atom for the Li−Fe−Ge compounds, while higher moments of 1.63−2.90 μ_B/Fe atom were theoretically predicted. Experimental (in)validation addresses the issue of inaccuracy in determining material properties *in silico* only and helps to improve the prediction power of the computational models. This work underlines that the contribution of experimentalists continues to be valuable for the accurate determination of structure−property relationships in solid-state materials.

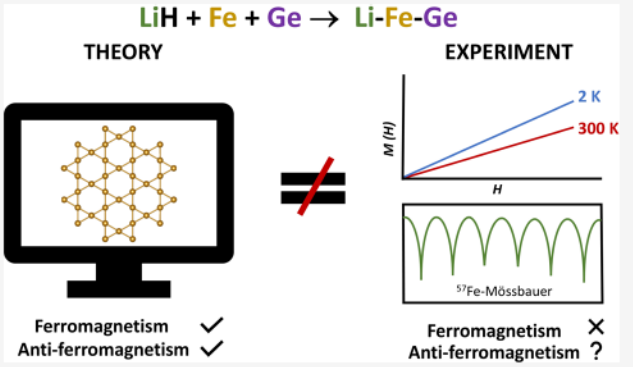

INTRODUCTION

Understanding the structure−property relationships in solid-state compounds is an important endeavor in the pursuit of technologically relevant materials. There exist various material classes of inorganic solids where the unique structural features afford them distinct properties. The Kagomé class of compounds is one such example, featuring a two-dimensional trihexagonal sublattice in their crystal structure.[1−3] The geometry of the Kagomé sublattice does not allow for a perfect antiferromagnetic alignment of spins, producing magnetic frustration that gives rise to unique electronic behavior and magnetic properties, including superconductivity, quantum spin liquid (QSL) behavior, and charge density wave (CDW) order.[4−10] The complex physics of Kagomé compounds has geared extensive research efforts toward elucidating their structure−property relationship, including the use of computational methods for the identification of suitable Kagomé candidates for applications such as superconductivity and quantum spin liquids.[11−15] For example, in the work by Meschke et al., machine learning (ML)- and density functional theory (DFT)-based analysis of ∼500 previously reported Kagomé compounds was performed to identify suitable QSL candidates.[11] The detailed report includes predictions of magnetic ground states and calculations of magnetic moments for the atoms forming the Kagomé sublattice in several Kagomé compounds. Another example is provided by the work of Jovanovic and Schoop, which demonstrates the use of chemical heuristics, local symmetry considerations, and DFT-based calculations for the prediction of band structures in Kagomé materials as a means of recognizing their unique magnetic properties.[12]

The past decade has seen a steep rise in the use of DFT- and ML-based predictions of inorganic material structures and properties for both known and novel chemical compositions.[16−24] Many databases, including the Open Quantum Material Database (OQMD)[25,26] and the Materials Project (MP)[27] database, provide insightful information about the material's structure, magnetic properties, and formation energy, among other properties. There are numerous examples in the literature for the predictions of new materials with targeted properties or predictions of novel properties for known compounds.[19−24] However, few reports provide

Received: September 16, 2024
Revised: December 2, 2024
Accepted: December 4, 2024
Published: December 18, 2024

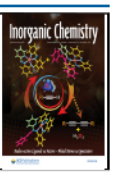

experimental validation or invalidation of the predicted properties.[28,29] Examples include the work by Singh et al., where the ML-predicted Curie temperature for the $(Zr_{0.16}Ce_{0.84})Fe_2$ and $(Zr_{0.94}Ce_{0.06})Fe_2$ pseudo-binaries was experimentally confirmed.[28] There also exist examples where DFT-based predictions have been experimentally proven incorrect.[11,30] For instance, an antiferromagnetic order in the $MgCo_6Ge_6$ Kagome germanide with a magnetic moment of 1.3 μ_B/Co atom was predicted by Meschke et al.,[11] while experimental results reveal Pauli paramagnetism.[30] While computational tools can be used for advancing the understanding of the material structure and properties, we believe that they cannot be developed independently of experimentation.[31,32] Experiments to (in)validate and improve the predictability of theoretical models are essential. Our work is an effort in this direction, where we experimentally explore the magnetism in three known Kagomé compounds in the Li−Fe−Ge systems, *i.e.*, $LiFe_6Ge_4$, $LiFe_6Ge_5$, and $LiFe_6Fe_6$, and test their predicted magnetic properties.[11,27]

The $LiFe_6Ge_4$, $LiFe_6Ge_5$, and $LiFe_6Ge_6$ compounds were first synthesized in the late 1970s and are known to contain a Kagomé network of Fe atoms.[33−35] The Materials Project database predicts ferromagnetic (FM) ground states for all three phases, with the magnetic moment of 2.41 μ_B, 1.63 μ_B, and 2.12 μ_B per Fe atom in $LiFe_6Ge_4$, $LiFe_6Ge_5$, and $LiFe_6Ge_6$, respectively.[27] Such values are comparable to the experimentally measured magnetic moment per Fe atom in the well-known permanent magnet $Nd_2Fe_{14}B$.[36,37] Another independent work by Meschke et al. also predicted ferromagnetic (FM) ground state with a magnetic moment of 2.83 μ_B/Fe atom in $LiFe_6Ge_6$ and an antiferromagnetic (AFM) ground state with a magnetic moment of 2.90 μ_B/Fe atom in $LiFe_6Ge_4$.[11] To the best of our knowledge, there are no experimental reports on the synthesis of polycrystalline powders of $LiFe_6Ge_4$ and $LiFe_6Ge_5$ or on their magnetic properties. The synthesis of $LiFe_6Ge_6$ using Li metal is reported,[33,38] and the measurement of magnetic properties performed on a polycrystalline sample of $LiFe_6Ge_6$ indicates a possibility of AFM ordering at $T > 300$ K.[38] The prediction of magnetically ordered ground states for the $LiFe_6Ge_4$, $LiFe_6Ge_5$, and $LiFe_6Fe_6$ Kagomé compounds and a lack of detailed experimental evidence inspired us to probe the magnetic properties of the Li−Fe−Ge compounds.

While measurement of properties using single crystals is ideal for the elucidation of the intrinsic properties of a material,[39] measurements on polycrystalline samples can provide valuable information and shed light on their bulk properties. Preparation of polycrystalline samples using traditional high-temperature ("heat-and-beat") methods is often diffusion-limited, leading to multiphase samples. This is an even greater challenge for the synthesis of $LiFe_6Ge_4$, $LiFe_6Fe_5$, and $LiFe_6Ge_6$ phases due to their compositional proximity, consistent with the lack of reports on the bulk synthesis of $LiFe_6Ge_4$ and $LiFe_6Ge_5$ using traditional routes.[33,34] While the polycrystalline sample of $LiFe_6Ge_6$ can be prepared, a large excess of Li, long annealing times, and post-treatment with water to remove excess Li are required to obtain the phase in high yield.[38] In this work, we utilize the hydride route for the facile synthesis of the $LiFe_6Fe_4$, $LiFe_6Fe_5$, and $LiFe_6Fe_6$ phases in the polycrystalline form, where the soft alkali metal precursor (Li) is replaced with powder-like reactive alkali metal hydride (LiH).[40−43] Since all the precursors for the hydride route are in the powder form, they can be weighed precisely, providing excellent compositional control, handy for the Li−Fe−Ge system where the three target phases exist within a narrow compositional space. The route also allows for the intimate mixing of precursors *via* ball milling, helping with diffusion limitation, and hence provides a notable alternative to the traditional synthesis route.

Herein, we report the successful synthesis of $LiFe_6Fe_4$, $LiFe_6Fe_5$, and $LiFe_6Fe_6$ phases in the polycrystalline form *via* the hydride route and the experimental characterization of their magnetic properties with the goal of testing the predicted magnetic properties. We present a comparison of the experimentally determined and theoretically predicted magnetic properties for $LiFe_6Ge_4$, $LiFe_6Ge_5$, and $LiFe_6Fe_6$.

EXPERIMENTAL SECTION

Chemicals. Iron powder (Fe, Alfa Aesar, 99.998%) and lithium hydride powder (LiH, Alfa Aesar, 99.4%) were used as received. Germanium pieces (Ge, Alfa Aesar, 99.999%) were ball-milled using a tungsten carbide (WC) ball mill container and two WC balls for 30 min to obtain a fine powder. Sample manipulations were conducted in a glovebox under a dry argon atmosphere, $p(O_2) < 1$ ppm and $p(H_2O) < 1$ ppm.

Synthesis. Synthesis of the samples was conducted *via* hydride route. Starting materials were weighed as powders in desired LiH, Fe, and Ge molar ratios (total weight: 0.3 g). The powders were loaded into a polycarbonate grinding set with a methacrylate grinding ball. The vial was sealed into two polyethylene bags under an argon atmosphere, taken out of the glovebox, and ball-milled using a SPEX mixer/mill 8000 M for 6 min. In the glovebox, the ball-milled powders were loaded into tantalum tubes (ID: 5.4 mm; OD: 6.4 mm) and sealed using an arc welder under an argon atmosphere. The Ta tubes were placed into a silica reactor, evacuated to a pressure of 3.0×10^{-5}–3.5×10^{-5} bar, and placed into a programmable high-temperature furnace. The silica reactor is equipped with Swagelok safety check valves to avoid overpressurizing the silica reactor due to hydrogen gas released during the reaction. The setup was heated from room temperature (RT) to 1023 K in 5 h, annealed for 12 h, and then cooled naturally to room temperature.

Powder X-ray Diffraction (PXRD). The purity of the synthesized sample was confirmed from powder X-ray diffraction using a Rigaku MiniFlex600 powder diffractometer with Cu Kα radiation (λ = 1.54051 Å) and a Ni Kβ filter. Data were collected on a zero-background plate holder in air at room temperature. Phase analysis was performed using the COD database incorporated into Match-3! software.[44] Rietveld refinement of the PXRD data was performed to accurately determine the impurity content in the synthesized samples using the GSAS II software package.[45]

High-Temperature Synchrotron Powder X-ray Diffraction (HT-PXRD). High-temperature X-ray diffraction data were collected at the synchrotron beamline 17-BM at the Advanced Photon Source (APS) at Argonne National Lab (ANL), λ = 0.24130 Å. A finely ground sample of $LiFe_6Ge_5$ and $LiFe_6Ge_6$ was filled into a 0.7 mm-outer diameter, thick-wall (0.1 mm) silica capillary and sealed under vacuum. The capillary was mounted into a secondary shield capillary on a sample stage equipped with two resistive microheaters and a thermocouple set as close as possible to the measurement area. Details of the setup can be found elsewhere.[46] Data were collected upon heating and cooling in the temperature range of 298 K−1173 K−298 K with a heating rate of 15 K/min and a cooling rate of 25 K/min, followed by fast cooling.

Magnetic Properties. Magnetic measurements were performed on ∼50 mg polycrystalline samples of $LiFe_6Ge_4$, $LiFe_6Ge_5$, and $LiFe_6Ge_6$ in a gelatin capsule inside a plastic straw using Quantum Design MPMS XL and MPMS3 SQUID magnetometers. DC magnetic susceptibility measurements were performed in applied fields of 0.005 T and 0.1 T in the 2−300 K temperature range. Field dependence of magnetization was measured in the 0−7 T range at 2 and 300 K.

https://doi.org/10.1021/acs.inorgchem.4c03925
Inorg. Chem. 2024, 63, 24697−24708

^{57}Fe Mössbauer Spectroscopy. Mössbauer spectroscopy measurements were performed using a SEE Co. conventional constant acceleration-type spectrometer in transmission geometry with a ^{57}Co(Rh) source, kept at room temperature. For the absorber, 20–40 mg of powders of the samples was mixed with a ZG-grade BN powder to ensure homogeneity. The absorber holder comprised two nested white Delrin cups. The driver velocity was calibrated by α-Fe foil, and all isomer shifts (IS) are quoted relative to the α-Fe foil at room temperature. A commercial software package, MossWinn,[47] was used to analyze the Mössbauer spectra in this work.

RESULTS AND DISCUSSION

Synthesis. Several loading molar ratios of LiH:Fe:Ge and temperature profiles were attempted to synthesize $LiFe_6Ge_4$, $LiFe_6Ge_5$, and $LiFe_6Ge_6$ in high yield. The hydride route was employed, where ball-milled powders of LiH, Fe, and Ge were taken in a desired molar ratio and heated at 1023 K for 12 h to produce crystalline samples of $LiFe_6Ge_4$, $LiFe_6Ge_5$, and $LiFe_6Ge_6$ with minimized amounts of secondary phases. The compounds were obtained as a dark-gray powder with a weight fraction of target phases exceeding 90 wt %: 92.9 wt % for $LiFe_6Ge_4$ (containing 7.1 wt % $LiFe_6Ge_5$), 91.0 wt % for $LiFe_6Ge_5$ (containing 9.0 wt % $LiFe_6Ge_4$), and 100 wt % for $LiFe_6Ge_6$ according to Rietveld refinement of PXRD data (Figures 1 and S1). The unit cell dimensions of hydride-synthesized phases are comparable to those obtained *via* single-crystal X-ray diffraction (SC-XRD) for $LiFe_6Ge_4$, $LiFe_6Ge_5$, and $LiFe_6Ge_6$ synthesized from elements.[33−35]

Figure 2 shows the Li−Fe−Ge compositional phase space with the optimized (filled circles) and other attempted (shaded regions) loading compositions used for the synthesis *via* the hydride route, whereas the actual phase compositions, *i.e.*, $LiFe_6Ge_4$, $LiFe_6Ge_5$, and $LiFe_6Ge_6$, are shown as open circles. Excess Li and Ge are required for synthesis, as indicated by the difference in optimized *vs* actual composition in Figure 2. The optimized loading molar ratios for $LiFe_6Ge_4$, $LiFe_6Ge_5$, and $LiFe_6Ge_6$ are LiH:Fe:Ge = 2.8:6:4.1, 2.3:6:5.2, and 2.2:6:6.1, respectively, signifying a need for 2.2- to 2.8-fold excess of LiH and a slight excess of Ge. We hypothesize that the need for excess Li and Ge may be due to slight oxidation of LiH and/or reaction of Ge powder with the reaction vessel (Ta tube); however, no Ta−Ge impurities were observed in PXRD post-synthesis. Alternatively, Li-rich compositions might be required for the formation of the low-melting Li−Ge binaries[48,49] that function as a flux and promote Fe incorporation toward the synthesis of the Li−Fe−Ge ternaries. The initial work on the synthesis of single crystals of $LiFe_6Ge_4$ and $LiFe_6Ge_5$ also reports the need for excess Li (6-fold) and Ge (2 to 4-fold) to avoid the formation of a mixture of ternaries.[34] Crystals of the $LiFe_6Ge_4$ and $LiFe_6Ge_5$ ternaries form along with Li and Li−Ge binaries, consistent with the considerable Li and Ge excess used. Li and Li−Ge phases were washed using water, leaving behind shiny silver crystals of the targeted Li−Fe−Ge ternary.[34] For $LiFe_6Ge_6$, single crystals can be synthesized in high yield, albeit the crystals obtained have the dimension of 0.04 mm × 0.01 mm × 0.5 mm,[33] suitable for SC-XRD analysis but too small to examine material properties. The preparation of $LiFe_6Ge_4$ and $LiFe_6Ge_5$ as polycrystalline powders has not been reported yet. Preparation of the polycrystalline sample of $LiFe_6Ge_6$ using Li is reported,[38] where substantial excess of Li (Li:Fe:Ge = 6:6:6, *i.e.*, 6-fold Li excess) and significantly longer annealing periods (168 h with Li *vs* 12 h with LiH) are required. The excess Li needs to be removed by washing the synthesized powder with water, adding an additional step to obtain a single-phase sample of $LiFe_6Ge_6$. The above discussion clearly highlights the advantage and suitability of the hydride route for the facile preparation of the polycrystalline powder of Li−Fe−Ge phases in high yield, facilitating the evaluation of their bulk properties.

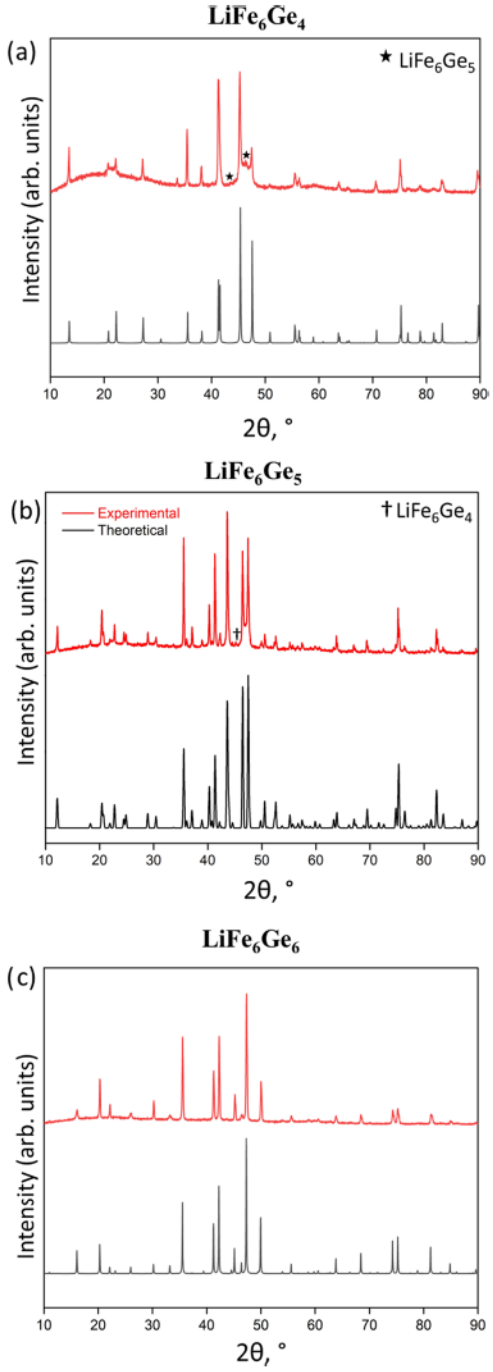

Figure 1. Experimental (red) and calculated (black) powder X-ray diffraction data for (a) $LiFe_6Ge_4$, (b) $LiFe_6Ge_5$, and (c) $LiFe_6Ge_6$, with diffraction peaks for the impurity phases marked.

Hydride reactions performed with stoichiometric molar ratios of LiH, Fe, and Ge powders corresponding to the phase compositions result in the synthesis of the ternaries, albeit with the formation of secondary phases such as binary $Fe_{3+x}Ge_2$ and Ge. The LiH:Fe:Ge = 1:6:4 stoichiometric loading results in the synthesis of $Fe_{3.34}Ge_2$ as the major phase along with the synthesis of $LiFe_6Ge_5$ instead of the target $LiFe_6Ge_4$. The

https://doi.org/10.1021/acs.inorgchem.4c03925
Inorg. Chem. 2024, 63, 24697−24708

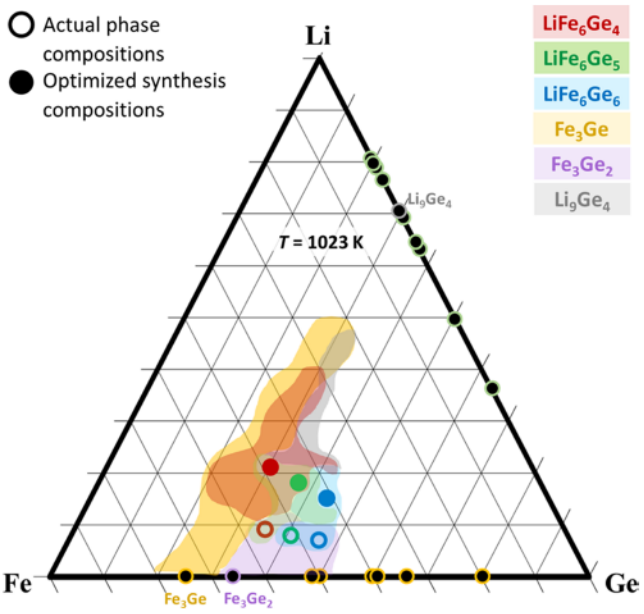

Figure 2. Compositional diagram for the Li−Fe−Ge ternary system, representing the optimized synthesis composition (filled circles) and phase composition (open circles) for $LiFe_6Ge_4$ (red), $LiFe_6Ge_5$ (green), and $LiFe_6Ge_6$ (blue). The shaded regions include all the compositions where the respective phases are observed by PXRD: $LiFe_6Ge_4$ (red), $LiFe_6Ge_5$ (green), $LiFe_6Ge_6$ (blue), $Fe_{3+x}Ge_2$ (purple), Fe_3Ge (yellow), and Li_9Ge_4 (gray). The difference between the optimized composition and phase composition indicates that excess Li and Ge are needed to maximize the yield of target $LiFe_6Ge_4$, $LiFe_6Ge_5$, and $LiFe_6Ge_6$ compounds.

molar ratio LiH:Fe:Ge = 1:6:5 results in a minor amount of $LiFe_6Ge_5$, while the major phases obtained are $LiFe_6Ge_6$ and $Fe_{3.34}Ge_2$. Finally, the molar ratio LiH:Fe:Ge = 1:6:6 results in the synthesis of $LiFe_6Ge_6$, along with considerable fractions of Ge and Fe_3Ge_2.

Other compositions with variable Li excess and Fe:Ge ratios were also attempted (composition within shaded regions in Figure 2). The different colors of the shaded region represent the compositions in the Li−Fe−Ge phase space, where the formation of $LiFe_6Ge_4$ (red), $LiFe_6Ge_5$ (green), $LiFe_6Ge_6$ (blue), $Fe_{3+x}Ge_2$ (purple), Fe_3Ge (yellow), and Li_9Ge_4 (gray) phases was observed. As seen in Figure 2, Li-poor compositions (less than 1.7-fold excess) promoted the formation of the $Fe_{3+x}Ge_2$ phase (purple region). For compositions that are Li-rich (more than 2.8-fold excess), the formation of the Fe_3Ge (yellow region) and Li_9Ge_4 (gray region) binaries was observed. Li-rich compositions also seem to favor the synthesis of $LiFe_6Ge_4$ (red region) together with Fe_3Ge and/or Li_9Ge_4. A 1.7- to 2.8-fold Li excess turned out to be optimal for the synthesis, providing the highest wt % of the targeted Li−Fe−Ge ternary compounds. Maintaining the optimal Li excess, the yield of the desired ternary phase was found to be highly sensitive to the Fe:Ge ratio due to the compositional proximity of $LiFe_6Ge_4$, $LiFe_6Ge_5$, and $LiFe_6Ge_6$. Ge-poor compositions, *i.e.*, LiH:Fe:Ge = (1.7−2.8):6:(2.6−4.0), resulted in the $LiFe_6Ge_4$ along with Fe_3Ge. The Ge-rich compositions, *i.e.*, LiH:Fe:Ge = (1.7−2.8):6:(6.0−6.3), form $LiFe_6Ge_6$ along with Ge. For the compositions in the middle, *i.e.*, LiH:Fe:Ge = (1.7−2.8):6:(4.0−6.0), a mixture of either $LiFe_6Ge_4$ and $LiFe_6Ge_5$ [for Fe:Ge = 6:(4−5)] or $LiFe_6Ge_5$ and $LiFe_6Ge_6$ [for Fe:Ge = 6:(5−6)] is obtained. For example, for the LiH:Fe:Ge = 2.2:6:4.4 loading composition, a mixture of $LiFe_6Ge_4$ and $LiFe_6Ge_5$ was synthesized, and when the precursors were taken in the LiH:Fe:Ge = 2:6:5.8 molar ratio, a mixture of $LiFe_6Ge_5$ and $LiFe_6Ge_6$ was obtained. Notably, all three ternary compounds are not observed in the same sample.

Attempts at optimizing other reaction parameters, such as temperatures and annealing times were also made but proved

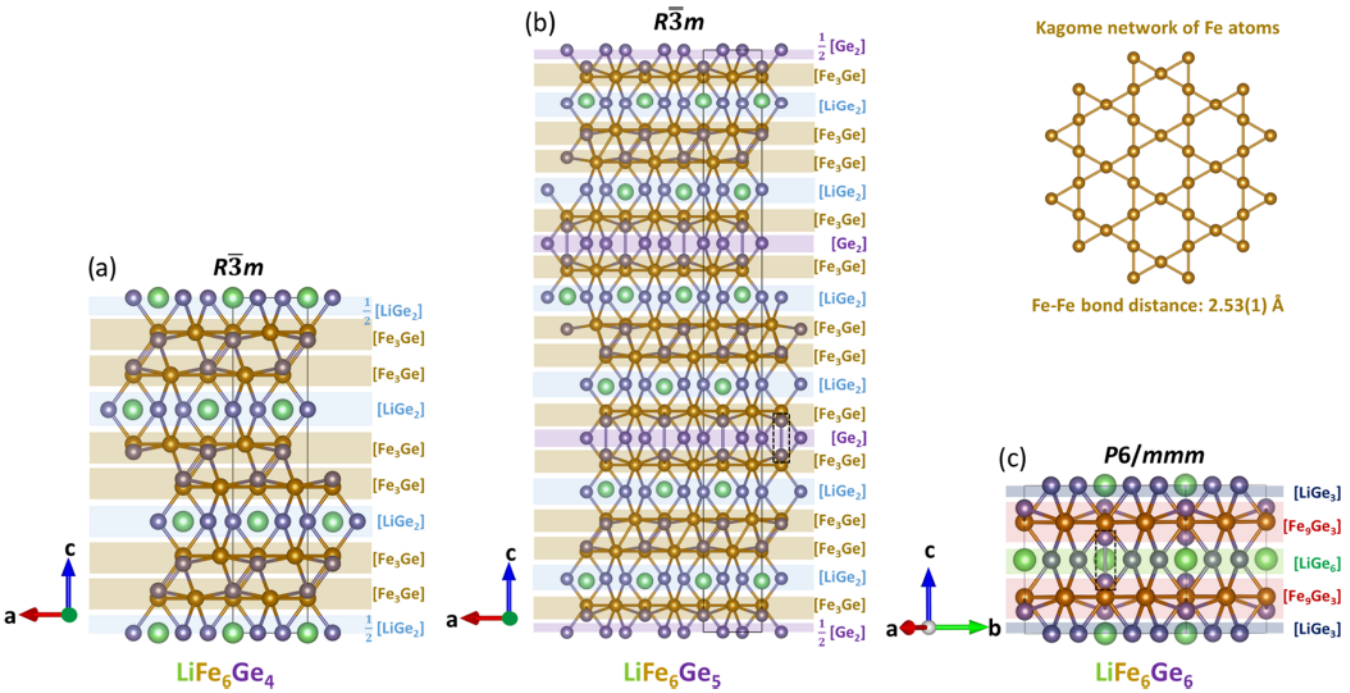

Figure 3. Crystal structure of (a) $LiFe_6Ge_4$, (b) $LiFe_6Ge_5$, and (c) $LiFe_6Ge_6$ with a breakdown of the layers building their 3-dimensional structures. Top right corner: Kagomé network of Fe atoms featured in all three phases.

https://doi.org/10.1021/acs.inorgchem.4c03925
Inorg. Chem. 2024, 63, 24697−24708

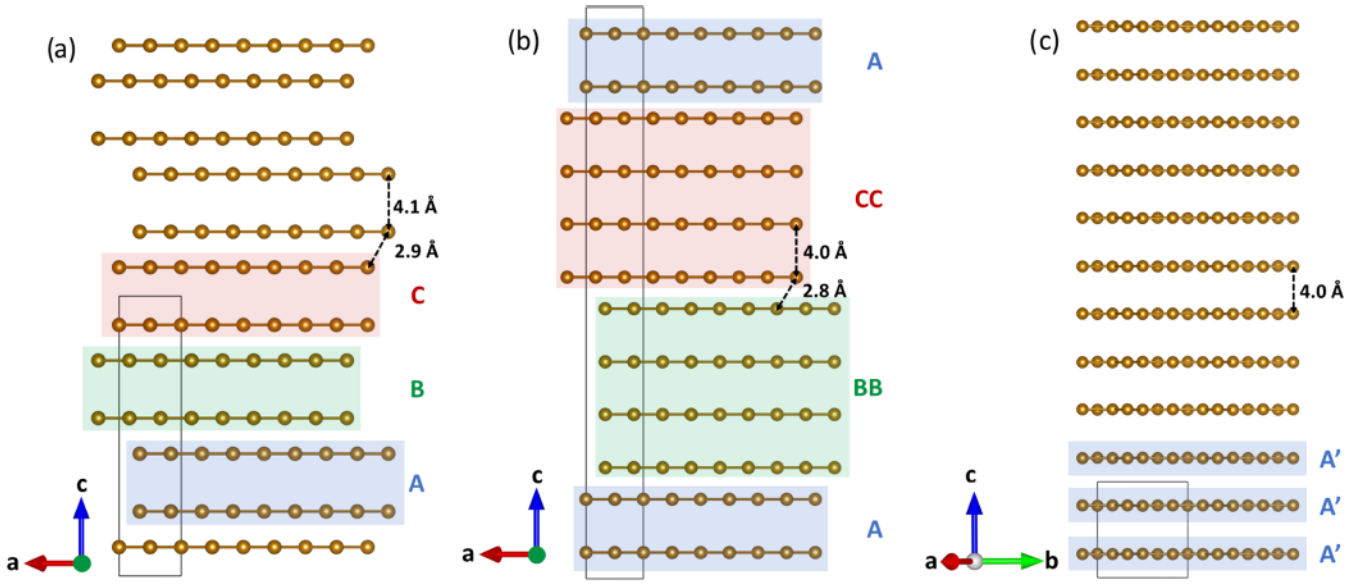

Figure 4. Stacking arrangement of Fe layers in (a) $LiFe_6Ge_4$, (b) $LiFe_6Ge_5$, and (c) $LiFe_6Ge_6$ along the *c* direction. The Fe−Fe bond distance within the Kagomé layers is 2.53(1) Å, whereas the out-of-plane Fe−Fe bond distance is in the range of 2.8−4.1 Å, as marked in the figure.

ineffective. When the synthesis temperature was lowered to 873 K, it led to a decrease in the crystallinity of the ternary phase, evident from the slight broadening of diffraction peaks in the PXRD pattern, while increasing the reaction temperature to 1173 K did not improve the crystallinity and promoted the formation of the $Fe_{3.4}Ge_2$ and Fe_3Ge binaries. Moreover, the variation in the synthesis temperature does not eliminate the formation of side phases. Adjusting the annealing time had no impact on the outcome of the reactions and, hence, was held constant at 12 h.

Overall, for all compositions in the LiH:Fe:Ge = (1.7−2.8):6:(2.6−6.3) range, $LiFe_6Ge_4$, $LiFe_6Ge_5$, and/or $LiFe_6Ge_6$ can be synthesized but are either obtained as a mixture of ternaries or accompanied by Fe−Ge or elemental Ge as secondary phases. While the close compositional proximity of $LiFe_6Ge_4$, $LiFe_6Ge_5$, and $LiFe_6Ge_6$ posed limitations to synthesis optimization, the precise compositional control afforded by the hydride route allows for the fine tuning of the LiH:Fe:Ge ratio, eventually permitting the synthesis of $LiFe_6Ge_4$, $LiFe_6Ge_5$, and $LiFe_6Ge_6$ in high yield (>90 wt %). Our work provides the first example of a synthetic route for the preparation of polycrystalline powders of $LiFe_6Ge_4$ and $LiFe_6Ge_5$ and a facile alternative for the synthesis of $LiFe_6Ge_6$.

Crystal Structure. The crystal structures of the $LiFe_6Ge_4$, $LiFe_6Ge_5$, and $LiFe_6Ge_6$ phases were determined in earlier reports through single-crystal X-ray diffraction (SC-XRD) study.[33−35] $LiFe_6Ge_4$ and $LiFe_6Ge_5$ phases crystallize in the trigonal space group $R\bar{3}m$ (*No* 166) with a = 5.05 Å, c = 19.66 Å, Z = 3 for $LiFe_6Ge_4$ and a = 5.05 Å, c = 43.64 Å, Z = 6 for $LiFe_6Ge_5$. The $LiFe_6Ge_6$ phase displays a hexagonal structure (a = 8.74 Å, c = 8.03 Å, Z = 3) in the *P6/mmm* space group. The crystal structure of the $LiFe_6Ge_4$, $LiFe_6Ge_5$, and $LiFe_6Ge_6$ phases can be described as a 3-dimensional covalent network comprising Fe and Ge atoms, with electropositive Li occupying the voids created within the covalent network (Figure 3).

The crystal structures of the three phases show striking similarities, which can be attributed to the compositional proximity and similar bonding interactions. A layer-by-layer breakdown of the three-dimensional (3D) structures of $LiFe_6Ge_4$, $LiFe_6Ge_5$, and $LiFe_6Ge_6$ phases allows for easy identification of their structural relations (as shown in Figure 3). Figure 3a,b shows that $LiFe_6Ge_4$ and $LiFe_6Ge_5$ phases are built from the same [$LiGe_2$] and [Fe_3Ge] layers highlighted in blue and brown, respectively. The added Ge atoms in $LiFe_6Ge_5$ are accommodated as [Ge_2] layers (highlighted in purple in Figure 3b) that are sandwiched between the [Fe_3Ge] layers. Within this Ge layer in the structure of $LiFe_6Ge_5$, Ge dumbbells form with a Ge−Ge distance of 2.63 Å (black dashed box in Figure 3b). Such Ge dumbbells also appear in the structure of $LiFe_6Ge_6$ (Ge−Ge distance: 2.43 Å, black dashed box in Figure 3c). Unlike $LiFe_6Ge_5$, the added Ge in $LiFe_6Ge_6$ is accommodated within the [Li−Ge] layers instead of separate [Ge_2] layers, resulting in the Ge-rich composition of the [Li−Ge] layers in $LiFe_6Ge_6$ compared to $LiFe_6Ge_4$ and $LiFe_6Ge_5$, *i.e.*, [$LiGe_6$] and [$LiGe_3$] in $LiFe_6Ge_6$ *vs* [$LiGe_2$] in $LiFe_6Ge_4$ and $LiFe_6Ge_5$. In other words, the [$LiGe_6$] and [$LiGe_3$] layers in $LiFe_6Ge_6$ (highlighted in green and dark blue in Figure 3c) are similar to the [$LiGe_2$] layers in $LiFe_6Ge_4$ and $LiFe_6Ge_5$, except for the extra Ge dumbbells.

In addition to possessing common layered fragments that build the 3D structure, all three compounds also feature a Kagomé network of Fe atoms with an Fe−Fe bond distance of 2.53(1) Å (represented in the top right corner in Figure 3). The structural similarities in $LiFe_6Ge_4$, $LiFe_6Ge_5$, and $LiFe_6Ge_6$ are well reflected in the bonding environments around the Li, Fe, and Ge atoms (Figure S2). There are coordination environments common to all three structures, such as the hexagonal bipyramidal coordination of Li with Ge (Figure S2a) and the trigonal prismatic coordination of Ge with Fe (Figure S2f). A few coordination environments in $LiFe_6Ge_4$ and $LiFe_6Ge_6$ are closely related yet distinct. For example, Fe atoms in $LiFe_6Ge_6$ are 10-coordinated to Ge atoms, as shown in Figure S2b. In $LiFe_6Ge_4$, similar coordination is observed, but Fe atoms have one less adjacent Ge atom, resulting in a 9-coordinated Fe atom (Figure S2c). Apart from the common trigonal prismatic coordination by 6 Fe atoms, Ge atoms display different coordination environments in the structures of Li−Fe−Ge ternaries. In $LiFe_6Ge_6$, Ge atoms form dumbbells,

https://doi.org/10.1021/acs.inorgchem.4c03925
Inorg. Chem. 2024, 63, 24697−24708

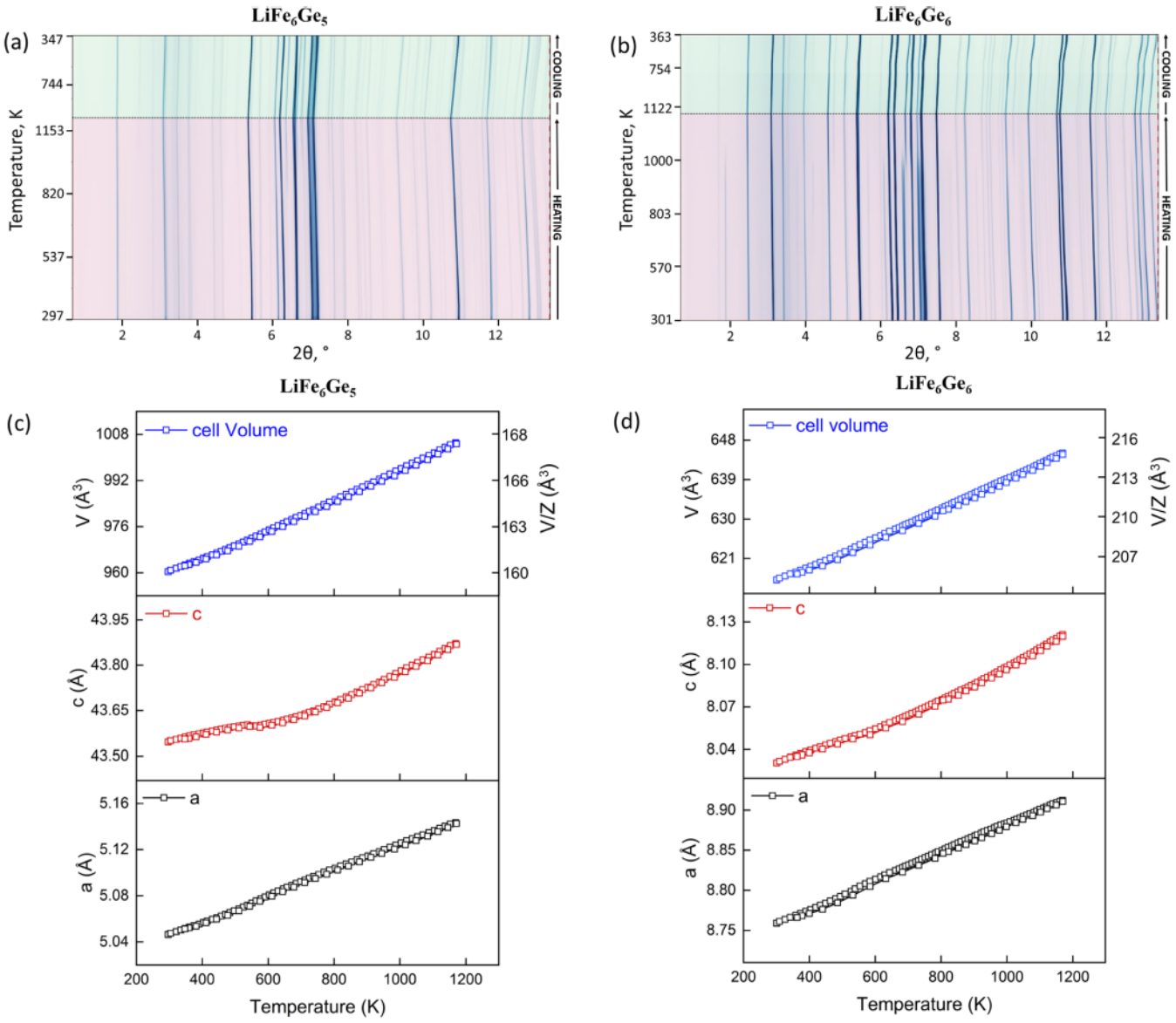

Figure 5. High-temperature *in situ* synchrotron PXRD data for $LiFe_6Ge_5$ and $LiFe_6Ge_6$. Waterfall plots for (a) $LiFe_6Ge_5$ and (b) $LiFe_6Ge_6$ powdered samples upon heating them from 298 to 1173 to 298 K. The vertical lines represent diffraction peaks in the PXRD at a given value of 2θ (λ = 0.24130 Å). Cell parameters a and c and cell volume V for (c) $LiFe_6Ge_5$ and (d) $LiFe_6Ge_6$ plotted as a function of temperature during the heating and cooling cycles.

where each Ge is, in turn, coordinated to 6 Fe atoms, as shown in Figure S2d. These Ge dumbbells are absent in $LiFe_6Ge_4$ (as also seen in Figure 3), where Ge is instead bonded to 9 Fe atoms (Figure S2e). Interestingly, all three Ge coordination environments, with the trigonal prismatic configuration being common for both $LiFe_6Ge_4$ and $LiFe_6Ge_6$, are found in the structure of the $LiFe_6Ge_5$ phase, demonstrating that $LiFe_6Ge_5$ is a structural hybrid of $LiFe_6Ge_4$ and $LiFe_6Ge_6$. Going from $LiFe_6Ge_4$ to $LiFe_6Ge_5$ and $LiFe_6Ge_6$, the structure of the compounds transforms to accommodate the added Ge while maintaining certain common structural motifs, resulting in crystal structures that are remarkably alike.

Figure 4 compares the stacking of the Kagomé layers of Fe atoms in $LiFe_6Ge_4$, $LiFe_6Ge_5$, and $LiFe_6Ge_6$. The Fe layers pile along the c direction with different stacking arrangements (Figure 4). In $LiFe_6Ge_4$, a relative shift of Fe atoms is observed after every two layers, establishing an [*ABC*] stacking pattern (Figure 4a). A similar stacking is seen in $LiFe_6Ge_5$, except for a shift every four Fe layers instead of two following the [*AABBCC*] stacking arrangement (Figure 4b). No relative shift exists in $LiFe_6Ge_6$, as the iron layers stack precisely above each other along the c-axis (Figure 4c). In $LiFe_6Ge_6$, the Fe–Fe distance between adjacent Fe layers is 4.0 Å, while in the case of $LiFe_6Ge_4$ and $LiFe_6Ge_5$, there are shorter distances of 2.8–2.9 Å and longer distances of 4.0–4.1 Å between the adjacent Fe layers. The wider spacing between the Fe layers accommodates the [$LiGe_2$], [$LiGe_3$], and [$LiGe_6$] layers in $LiFe_6Ge_4$, $LiFe_6Ge_5$, and $LiFe_6Ge_6$, respectively. In the case of $LiFe_6Ge_5$, the extra Ge atoms are also accommodated within this space (Figure 3b).

In summary, the crystal structures of $LiFe_6Ge_4$, $LiFe_6Ge_5$, and $LiFe_6Ge_6$ display remarkable similarity and evolve as the composition becomes richer in Ge. All three compounds contain a Kagomé layer of Fe atoms and show a different stacking arrangement of Fe-Kagomé layers in their crystal structure.

https://doi.org/10.1021/acs.inorgchem.4c03925
Inorg. Chem. 2024, 63, 24697–24708

Thermal Stability by HT-PXRD. High-temperature *in situ* synchrotron PXRD data were collected for the samples of $LiFe_6Ge_5$ (containing 9.0 wt % $LiFe_6Ge_4$) and $LiFe_6Ge_6$ (containing 11.9 wt % $LiFe_6Ge_5$). For both samples, the major phase remains the same; thus, no significant changes in the PXRD data were noticed upon heating and cooling the samples in the 298−1173−298 K range, suggesting the phases to be thermally stable up to 1173 K (Figure 5a,b). For the $LiFe_6Ge_6$ sample, while the diffraction peaks for the ternary remain intact in the entire temperature range, the simultaneous disappearance of diffraction peaks at 1.9 and 6.6° and the appearance of a diffraction peak at 6.7° are observed at ∼1000 K. This corresponds to the decomposition of $LiFe_6Ge_5$ (present as an impurity from the beginning) to $Fe_{3.34}Ge_2$ and presumably with Li−Ge binaries and Ge. However, no Li−Ge binary or Ge diffraction peaks were observed during the entire measurement. According to Rietveld refinement, after HT-PXRD, a sample of $LiFe_6Ge_6$ contains 8 wt % of $Fe_{3.34}Ge_2$ in addition to the $LiFe_6Ge_6$ major phase, while a sample of $LiFe_6Ge_5$ contains 10 wt % of $Fe_{3.34}Ge_2$ and 6 wt % of $LiFe_6Ge_6$ in addition to $LiFe_6Ge_5$ as a major phase (84 wt %).

Figure 5c,d represents the plots for unit cell parameters (a, c) and unit cell volume (V) for $LiFe_6Ge_5$ and $LiFe_6Ge_6$ as a function of temperature. The unit cell parameters determined from Rietveld refinement of the HT-PXRD data show a nearly linear increase with temperature and no hysteresis for the heating/cooling cycle in the 298−1173−298 K range. However, the c parameter of $LiFe_6Ge_5$ shows a nonlinear increase with temperature (Figure 5c, red curve). The positive thermal expansion is evident from the shifting of the diffraction peaks to the left upon heating due to unit cell expansion and to the right upon the cooling cycle due to unit cell contraction (Figure 5a,b). The coefficients of thermal expansion (CTE) were calculated from linear fits of the data shown in Figure 5c,d using eqs 1−3

$$\mathrm{CTE}(a) = \frac{\mathrm{d}a}{\mathrm{d}T} \times \frac{1}{a} \tag{1}$$

$$\mathrm{CTE}(c) = \frac{\mathrm{d}c}{\mathrm{d}T} \times \frac{1}{c} \tag{2}$$

$$\mathrm{CTE}(V) = \frac{dV}{d\mathrm{T}} \times \frac{1}{V} \tag{3}$$

The coefficients of thermal expansion are CTE (a) = 22.3 × 10^{-6} K^{-1}, CTE (c) = 8.2 × 10^{-6} K^{-1}, and CTE (V) = 57.4 × 10^{-6} K^{-1} for $LiFe_6Ge_5$ and CTE (a) = 20.4 × 10^{-6} K^{-1}, CTE (c) = 12.8 × 10^{-6} K^{-1}, and CTE (V) = 54.4 × 10^{-6} K^{-1} for $LiFe_6Ge_6$. If CTE(c) for $LiFe_6Ge_5$ is calculated in the 700−1173 K range, where a linear dependence of c with temperature is observed (Figure 5c, red curve), the value increases to CTE (c) = 11.8 × 10^{-6} K^{-1}. CTEs are remarkably similar for both phases.

In conclusion, the *in situ* HT-PXRD study reveals $LiFe_6Ge_5$ and $LiFe_6Ge_6$ phases to be thermally stable up to 1173 K and possess positive coefficients of thermal expansion, which are similar between the two phases. As a broader outlook, *in situ* HT-PXRD analysis of materials is crucial to understanding their thermal stability and behavior. Knowledge of a compound's decomposition temperature and pathway can be insightful in determining the synthetic parameters for growing crystals from the melt *via* Bridgman or Czochralski methods or from solutions using reactive fluxes, allowing investigation of the material structure and properties.

Magnetic Properties. Given the prediction of a ferromagnetic (FM) ground state in the $LiFe_6Ge_4$, $LiFe_6Ge_5$, and $LiFe_6Ge_6$ Kagomé compounds and also antiferromagnetic (AFM) ground states in $LiFe_6Ge_4$ by Meschke et al., we were interested in investigating the magnetic properties of these three compounds.[11,27] From the above-mentioned studies, a magnetic moment of 1.63−2.90 μ_B per Fe atom was predicted for these compounds, the value comparable to experimentally determined Fe magnetic moments in $Nd_2Fe_{14}B$.[11,27,36] Moreover, the structurally related Kagomé compounds FeGe and RFe_6Ge_6 (R = Mg, Sc, Ti, Nb, Lu, Hf, Zr, Yb) display AFM ordering, well established from magnetic susceptibility measurements, field-dependent magnetization, neutron diffraction studies, and Mössbauer spectroscopy.[50−57] In all RFe_6Ge_6 compounds that crystallize in the $HfFe_6Ge_6$ structure type, the Fe atoms within a single layer order ferromagnetically, but adjacent Fe layers order antiferromagnetically at temperatures significantly above room temperature (T_N ∼ 400 to 520 K).[50−57] The magnetic moment per Fe atom in this 1−6−6 family of compounds was found to be appreciably high, around 1−2 μ_B at 2 K, as determined from neutron diffraction data,[55,56] and comparable to the predicted magnetic moment per Fe atom in $LiFe_6Ge_6$.[11,27] RFe_6Ge_6 compounds containing a nonmagnetic R metal (R = Sc, Lu, Ti, Zr, Nb) display AFM ordering temperature T_N > 300 K and the value of Fe moment increases with an increase in the valency of R.[52,55] For example, trivalent Sc (T_N = 497 K for $ScFe_6Ge_6$) and Lu (T_N = 471 K for $LuFe_6Ge_6$), tetravalent Ti (T_N = 518 K for $TiFe_6Ge_6$) and Zr (T_N = 508 K for $ZrFe_6Ge_6$), and pentavalent Nb (T_N = 561 K for $NbFe_6Ge_6$) show a clear increase in T_N with an increase in R valency. However, divalent Mg deviates from this trend as T_N = 501 K is observed for $MgFe_6Ge_6$. While the magnetic properties of RFe_6Ge_6 compounds containing divalent to pentavalent R metals have been studied,[50−57] magnetic properties for compounds with monovalent R metals are not well explored. This further motivated us to investigate the magnetism in $LiFe_6Ge_6$ (R = monovalent Li).

Figure 6 displays magnetization per Fe atom (μ_B) as a function of the applied magnetic field for the $LiFe_6Ge_4$, $LiFe_6Ge_5$, and $LiFe_6Ge_6$ phases. A linear dependence of magnetization on the field is observed for $LiFe_6Ge_4$ and $LiFe_6Ge_5$ at 2 and 300 K. The linear dependence together with an overall low magnetization of ∼0.04 μ_B per Fe atom at 7 T reveals paramagnetism or antiferromagnetic (AFM) ordering at temperature above 300 K for the two phases (Figure 6a,b). For $LiFe_6Ge_6$, magnetization increases linearly with an increase in the field above 1T, once again suggesting paramagnetic behavior or AFM ordering above room temperature (Figure 6c). A nonlinear temperature dependence at a lower field for $LiFe_6Ge_6$ (0−1 T) at both 2 and 300 K indicates a small ferromagnetic contribution from impurity (Figure 6c) or AFM-like ordering above room temperature with a small FM component. Assuming Fe metal to be the ferromagnetic impurity, 0.46 wt % of Fe impurity (saturation moment M_S = 2.2 μ_B and saturation field H_S = 0.6 T) in $LiFe_6Ge_6$ can be estimated from a linear fit of the $M(H)$ curve above 1 T.

Molar magnetic susceptibility (χ) is positive and small in magnitude (∼0.02 emu/mol) for $LiFe_6Ge_4$ and $LiFe_6Ge_5$ (Figure S3a−d). Both zero field-cooled (ZFC) and field-cooled (FC) susceptibility show minuscule changes with temperature in the 2−300 K temperature range at 50 or 1000

https://doi.org/10.1021/acs.inorgchem.4c03925
Inorg. Chem. 2024, 63, 24697−24708

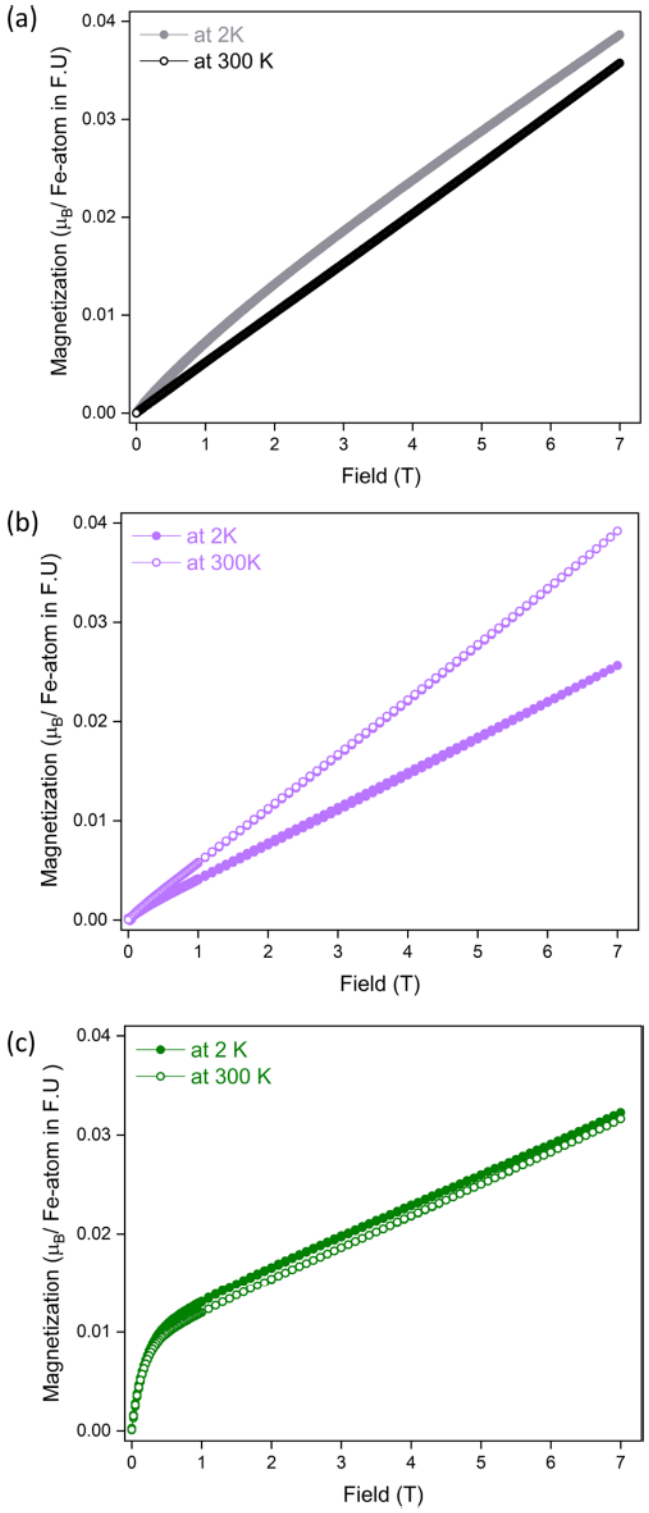

Figure 6. Plot of magnetization per mol of Fe atom (μ_B) as a function of the applied magnetic field at 2 and 300 K for (a)$LiFe_6Ge_4$, (b) $LiFe_6Ge_5$, and (c) $LiFe_6Ge_6$. Magnetic measurements were carried out on the samples of $LiFe_6Ge_4$ (containing 14 wt % $LiFe_6Ge_5$), $LiFe_6Ge_5$ (containing 13 wt % $LiFe_6Ge_6$), and $LiFe_6Ge_6$ (containing 4 wt % Ge).

Oe applied field (Figure S3b–d) in line with paramagnetism or antiferromagnetic ordering above room temperature. A larger difference in the ZFC and FC curves and overall large magnitude of susceptibility for $LiFe_6Ge_6$ concurs with a small FM component in $M(H)$, stemming from a ferromagnetic impurity in the sample or intrinsic to the phase (Figure S3a, green curves).

The direct current (dc) magnetization measurements were complemented by ^{57}Fe Mössbauer spectroscopy data collected at room temperature (297 K) (Figure 7). The data were

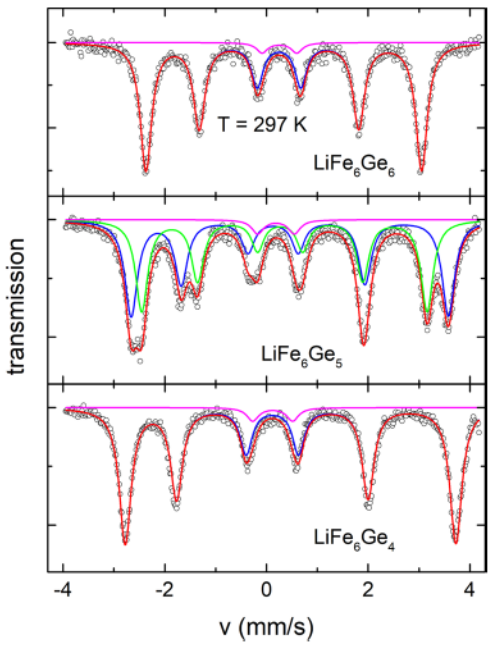

Figure 7. ^{57}Fe Mössbauer spectra of $LiFe_6Ge_4$ (bottom), $LiFe_6Ge_5$ (middle), and $LiFe_6Ge_6$ (top) at T = 297 K. Open symbols: experimental data; red lines: total fits; blue and green lines: sextets; and magenta lines: doublets.

successfully fitted with a sextet and a doublet for $LiFe_6Ge_6$ and $LiFe_6Ge_4$ and two sextets and a doublet for $LiFe_6Ge_5$. The results of the fits are listed in Table 1.

The sextets signify a static magnetic moment on Fe in $LiFe_6Ge_4$, $LiFe_6Ge_5$, and $LiFe_6Ge_6$. ^{57}Fe Mössbauer data for $LiFe_6Ge_4$ and $LiFe_6Ge_6$ data correspond to one magnetic Fe site, whereas there are two somewhat different sites in $LiFe_6Ge_5$, which is also in agreement with the single type of Fe-coordination environment in $LiFe_6Ge_4$ and $LiFe_6Ge_6$ and two types in $LiFe_6Ge_5$ (Figure S2b,c). By inspecting the quadrupolar splitting (QS) and hyperfine field (B_{hf}) values, it can be seen that just as $LiFe_6Ge_5$ is considered a structural hybrid of $LiFe_6Ge_4$ and $LiFe_6Ge_6$ (Figures 3 and S2), the local magnetic properties for the $LiFe_6Ge_5$ phase are also a hybrid of $LiFe_6Ge_4$ and $LiFe_6Ge_6$ as seen by the ^{57}Fe Mössbauer effect. From the B_{hf} values, we can roughly estimate the magnetic moment on Fe as ~1.3 μ_B for $LiFe_6Ge_4$, ~ 1.1 μ_B for $LiFe_6Ge_6$, and ~1.3 μ_B and ~1.2 μ_B for two Fe sites in $LiFe_6Ge_5$. Discussion of the proportionality coefficient between B_{hf} and the magnetic moment can be found elsewhere.[58] The observed doublets for the three phases correspond to a small fraction of some nonmagnetic Fe spins intrinsic to the major phases or from Fe-containing impurities.

A comparison of the ^{57}Fe Mössbauer data, *i.e.*, IS—isomer shift, QS—quadrupolar splitting, B_{hf}—hyperfine field, for the Li–Fe–Ge Kagomé compounds with the antiferromagnetic RFe_6Ge_6 (R = Mg, Sc, Ti, Nb) Kagomé compounds is provided in Table S1 in the Supporting Information. As seen in Table S1, similar IS and higher QS and B_{hf} values[52,55,59] are

https://doi.org/10.1021/acs.inorgchem.4c03925
Inorg. Chem. 2024, 63, 24697–24708

Table 1. Results of the Fits of the T = 297 K ^{57}Fe Mössbauer Spectra for $LiFe_6Ge_6$, $LiFe_6Ge_5$, and $LiFe_6Ge_4$[a]

compound	component	%	IS (mm/s)	QS (mm/s)	B_{hf} (T)	LW (mm/s)
$LiFe_6Ge_6$	sextet	96.2	0.293(1)	0.094(2)	16.845(7)	0.275(3)
	doublet	3.8	0.254(15)	0.68(3)		0.27[b]
$LiFe_6Ge_5$	sextet 1	50.4	0.294(1)	0.329(3)	19.39(1)	0.300(5)
	sextet 2	46.2	0.311(2)	0.083(3)	17.44(1)	0.289(5)
	doublet	3.4	0.19(1)	0.72(2)		0.28[b]
$LiFe_6Ge_4$	sextet	95.4	0.294(1)	0.358(1)	20.211(5)	0.283(2)
	doublet	4.6	0.122(8)	0.78(2)		0.28[b]

[a]IS—isomer shift, QS—quadrupolar splitting, Bhf—hyperfine field, and LW—line width. [b]Since the free parameter fit for doublets resulted in unreasonably narrow line widths, the doublet LW values were fixed at 0.27−0.28 mm/s (similar to those of sextets). Since doublets correspond to the minority (3−5%) phase, this restriction did not affect other results in any significant manner.

observed for Li−Fe−Ge phases compared to RFe_6Ge_6. The magnetic moment of 1.1−1.3 μ_B/Fe atom (at room temperature) obtained from the Mössbauer data for the Li−Fe−Ge compounds is similar to the magnetic moment of 1.1−1.7 μ_B/Fe atom in the RFe_6Ge_6 (R = Mg, Sc, Lu, Ti, Zr, Nb) compounds.[52,55,59] The above comparison serves as a strong indication of AFM ordering of Fe moieties in $LiFe_6Ge_4$, $LiFe_6Ge_5$, and $LiFe_6Ge_6$.

The collective analysis from the dc magnetization and Mössbauer data imply that the plausible magnetic state for $LiFe_6Ge_4$, $LiFe_6Ge_5$, and $LiFe_6Ge_6$ compounds would be antiferromagnetic with the ordering temperature above 300 K. From HT-PXRD data, a change of slope is observed at ∼575 K in the temperature-dependent curves for a and c unit cell parameters of $LiFe_6Ge_5$ and $LiFe_6Ge_6$ (Figure 5c,d). We hypothesize that this change of slope might be a result of structural changes brought about by magnetic ordering in these materials, suggesting an antiferromagnetic ordering temperature, T_N ∼ 575 K, for $LiFe_6Ge_5$ and $LiFe_6Ge_6$.

The experimental investigation of magnetic properties of $LiFe_6Ge_4$, $LiFe_6Ge_5$, and $LiFe_6Ge_6$ reveals antiferromagnetic (AFM) ordering at T > 300 K, which agrees with the prediction of the AFM ground state in $LiFe_6Ge_4$ by Meschke et al. but contradicts with the prediction of the ferromagnetic (FM) grounds state in $LiFe_6Ge_6$ by the same authors.[11] The experimental finding also conflicts with the predicted FM ground states for the three compounds in the Materials Project database.[27] Additionally, while the Materials Project database and the work by Meschke et al. calculate a magnetic moment of 2.41−2.90 μ_B/Fe atom, 1.63 μ_B/Fe atom, and 2.12−2.83 μ_B/Fe atom in $LiFe_6Ge_4$, $LiFe_6Ge_5$, and $LiFe_6Fe_6$ respectively,[11,27] our ^{57}Fe Mössbauer data reveal a lower magnetic moment of ∼1.1−1.3 μ_B/Fe atom for the three phases. The above discussion highlights the inconsistency between the experimentally measured and theoretically predicted magnetic properties of the $LiFe_6Ge_4$, $LiFe_6Ge_5$, and $LiFe_6Fe_6$ Kagomé compounds. We propose two possible reasons for such an inconsistency:

(1) Theoretical methods used to calculate magnetic properties do not fully capture the complexity of the electronic structure and magnetic ordering in these compounds, averting modeling of factors like spin frustration of the triangular lattice, symmetry-based constraints, or electron correlations within a material. Another 1−6−6 Kagomé germanide was analyzed in the work by Meschke et al., where a mismatch between measured and predicted magnetic properties is revealed is $MgCo_6Ge_6$.[11] An AFM ground state with a magnetic moment of 1.3 μ_B/Co atom was predicted for $MgCo_6Ge_6$; however, experimental measurements of magnetization, resistivity, and heat capacity all reveal Pauli paramagnetism in $MgCo_6Ge_6$.[30] The above explanation emphasizes the need for experimental probing of the predicted magnetism to help refine and improve the computational methodology, ultimately leading to predictions of material properties with greater accuracy.

(2) Since LiH is used for the synthesis of $LiFe_6Ge_4$, $LiFe_6Ge_5$, and $LiFe_6Ge_6$, one can speculate that an alteration of magnetic properties might occur due to H-incorporation into the structure of the Li−Fe−Ge ternaries. Examples where hydrogen incorporation (in the form of the hydride H-ion) alters magnetic properties are known among rare earth-containing intermetallics, for instance, CeNiSn, GdTiGe, and $Pr_{1-x}Gd_xScGe$. In the hydrogenated version of these stannides and germanides, hydride ions occupy tetrahedral (T_d) and octahedral (O_h) interstitial voids surrounded by the electropositive rare-earth metals. Hydrogen incorporation (in the form of H^-) alters the magnetic properties of the parent compounds.[60−63] The structures of $LiFe_6Ge_4$, $LiFe_6Ge_5$, and $LiFe_6Fe_6$ compounds lack such interstitial sites, in part due to the low Li content (Figures 3 and S2). As discussed earlier, Li is coordinated with Ge in a hexagonal bipyramidal fashion with an Li−Ge distance of 2.5−2.9 Å (Figure S2a), leaving no space to be filled by the H^- ion. Additionally, hydrogen incorporation in the RTX compounds to form $RTXH_y$ is achieved under high pressures of H_2 gas (∼10 bar),[62] which is not the case for the synthesis of the Li−Fe−Ge ternary phases. In the synthesis of $LiFe_6Ge_4$, $LiFe_6Ge_5$, and $LiFe_6Fe_6$, the LiH precursor decomposes to form Li and H_2 gas. The latter escapes through the permeable walls of the tantalum tube used as the reaction vessel.[64] Our previous research with antimonides suggests that H-incorporation is unlikely at conditions similar to those used for synthesizing $LiFe_6Ge_4$, $LiFe_6Ge_5$, and $LiFe_6Fe_6$.[42,43] Based on the above discussion, H-incorporation in the structure of $LiFe_6Ge_4$, $LiFe_6Ge_5$, and $LiFe_6Fe_6$ seems improbable.

Further investigation of high-temperature magnetic properties is required to confirm the AFM ordering states compellingly suggested by dc magnetization and ^{57}Fe Mössbauer measurements for $LiFe_6Ge_4$, $LiFe_6Ge_5$, and $LiFe_6Fe_6$. Additionally, neutron diffraction at variable temperatures can shed light on the magnetic properties of the Li−Fe−Ge Kagomé phases. Neutron diffraction can also be helpful in eliminating the possibility of H-incorporation in Li−Fe−Ge

https://doi.org/10.1021/acs.inorgchem.4c03925
Inorg. Chem. 2024, 63, 24697−24708

phases synthesized *via* the hydride route. Alternately, sizable single crystals of $LiFe_6Ge_4$, $LiFe_6Ge_5$, and $LiFe_6Ge_6$ can be grown using suitable methods (aided by the information obtained from *in situ* PXRD studies in this work) for the comparison of their properties to those of the hydride-synthesized phases. Nonetheless, the hydride route was successfully used herein for the preparation of polycrystalline powders of $LiFe_6Ge_4$, $LiFe_6Ge_5$, and $LiFe_6Fe_6$ compounds, enabling experimental characterization of their magnetic properties and testing of the theoretically predicted material properties of these Kagomé compounds.

CONCLUSIONS

The Kagomé germanides $LiFe_6Ge_4$, $LiFe_6Ge_5$, and $LiFe_6Fe_6$ were successfully synthesized *via* hydride route, providing an alternative route for the synthesis of the phases as polycrystalline powders. $LiFe_6Ge_4$, $LiFe_6Ge_5$, and $LiFe_6Fe_6$ were synthesized in high yields exceeding 90 wt %, allowing the investigation of their magnetic properties. Although the crystal structures of the Li−Fe−Ge ternary phases have been previously reported, we provide a detailed comparison of the structure of $LiFe_6Ge_4$, $LiFe_6Ge_5$, and $LiFe_6Fe_6$ in terms of stacking of [Fe−Ge] and [Li−Ge] layers rationalizing their structural similarities but also accounting for the differences as the phases become compositionally richer in Ge. The thermal stability of $LiFe_6Ge_5$ and $LiFe_6Fe_6$ was analyzed using the high-temperature *in situ* PXRD analysis, revealing both phases to be thermally stable up to 1173 K. The magnetic measurements performed in this work highlight the inconsistency between experimental and theoretical magnetic properties for $LiFe_6Ge_4$, $LiFe_6Ge_5$, and $LiFe_6Fe_6$. While previous computational studies predict ferromagnetic ground states in $LiFe_6Ge_4$, $LiFe_6Ge_5$, and $LiFe_6Fe_6$, experimental investigation *via* dc magnetization measurements and Mössbauer spectroscopy indicate antiferromagnetic ordering at temperatures above 300 K for all three. A magnetic moment of 1.1−1.3 μ_B/Fe atom estimated from Mössbauer spectroscopy is lower compared to the theoretically calculated values of 1.6−2.9 μ_B/Fe. High-temperature magnetization measurements and neutron diffraction studies are required to further confirm the antiferromagnetic ordering for $LiFe_6Ge_4$, $LiFe_6Ge_5$, and $LiFe_6Fe_6$, while high-temperature *in situ* PXRD data hint at $T_N \sim 575$ K.

Through our work, we highlight the need for experimental (in)validation of the theoretically predicted material properties, which is essential to assess the efficiency of computational methodologies and further improving predictive capabilities. The synergy between the experiment and theory is crucial for accurate elucidation of material properties. We believe that experimentalists will continue to play a pivotal role alongside theorists in predicting new materials, understanding their structure−property relationships and eventually realizing their potential for relevant technological applications.

ASSOCIATED CONTENT

Supporting Information

The Supporting Information is available free of charge at https://pubs.acs.org/doi/10.1021/acs.inorgchem.4c03925.

Rietveld refinement of laboratory PXRD data for $LiFe_6Ge_4$, $LiFe_6Ge_5$, and $LiFe_6Ge_6$, comprehensive representation of coordination environments of Li, Fe, and Ge in the Li−Fe−Ge ternaries, additional plots for the temperature- and field-dependent magnetic properties of $LiFe_6Ge_4$, $LiFe_6Ge_5$, and $LiFe_6Ge_6$, and comparison of the ^{57}Fe Mössbauer data of the Li−Fe−Ge ternaries to RFe_6Ge_6 (R = Mg, Sc, Lu, Ti, Zr, Nb) Kagome compounds (PDF)

AUTHOR INFORMATION

Corresponding Author

Julia V. Zaikina − *Department of Chemistry, Iowa State University, Ames, Iowa 50011, United States;* orcid.org/0000-0002-8755-1926; Email: yzaikina@iastate.edu

Authors

Aishwarya Mantravadi − *Department of Chemistry, Iowa State University, Ames, Iowa 50011, United States*

Raquel A. Ribeiro − *Department of Physics and Astronomy, Iowa State University, Ames, Iowa 50011, United States*

Sergey L. Bud'ko − *Department of Physics and Astronomy and Ames National Laboratory, US DOE, Iowa State University, Ames, Iowa 50011, United States;* orcid.org/0000-0002-3603-5585

Paul C. Canfield − *Department of Physics and Astronomy and Ames National Laboratory, US DOE, Iowa State University, Ames, Iowa 50011, United States*

Complete contact information is available at: https://pubs.acs.org/10.1021/acs.inorgchem.4c03925

Notes

The authors declare no competing financial interest.

ACKNOWLEDGMENTS

Financial support from the National Science Foundation (U.S.) Division of Materials Research (DMR-1944551) CAREER Award is gratefully acknowledged. The use of the Advanced Photon Source at Argonne National Laboratory (APS ANL) was supported by the U.S. Department of Energy, Office of Science, Office of Basic Energy Sciences, under Contract No. DE-AC02-06CH11357. Dr. W. Xu and Dr. A. Yakovenko at 17-BM at APS ANL are thanked for their help with high-temperature synchrotron PXRD data collection. The magnetization and Mössbauer measurements (RAR, SLB, PCC) were supported by the U.S. Department of Energy (DOE), Office of Science, Basic Energy Sciences, Materials Science and Engineering Division, through the Ames National Laboratory. Ames National Laboratory is operated for the U.S. DOE by Iowa State University under contract # DE-AC02-07CH11358.

REFERENCES

(1) Pati, S. K.; Rao, C. N. R. Kagome Network Compounds and Their Novel Magnetic Properties. *Chem. Commun.* 2008, 4683−4693.

(2) Yin, J. X.; Lian, B.; Hasan, M. Z. Topological Kagome Magnets and Superconductors. *Nature* 2022, *612*, 647−657.

(3) Wang, Y.; Wu, H.; McCandless, G. T.; Chan, J. Y.; Ali, M. N. Quantum States and Intertwining Phases in Kagome Materials. *Nat. Rev. Phys.* 2023, *5*, 635−658.

(4) Wang, H.; Liu, Y.; Gong, M.; Jiang, H.; Gao, X.; Ma, W.; Luo, J.; Ji, H.; Ge, J.; Jia, S.; Gao, P.; Wang, Z.; Xie, X. C.; Wang, J. Emergent Superconductivity in Topological-Kagome-Magnet/Metal Heterostructures. *Nat. Commun.* 2023, *14* (1), No. 6998.

(5) Riberolles, S. X. M.; Han, T.; Slade, T. J.; Wilde, J. M.; Sapkota, A.; Tian, W.; Zhang, Q.; Abernathy, D. L.; Sanjeewa, L. D.; Bud'ko, S. L.; Canfield, P. C.; McQueeney, R. J.; Ueland, B. G. New Insight into

Tuning Magnetic Phases of RMn_6Sn_6 Kagome Metals. *npj Quantum Mater.* **2024**, *9*, No. 42.
(6) Mielke, C.; Qin, Y.; Yin, J. X.; Nakamura, H.; Das, D.; Guo, K.; Khasanov, R.; Chang, J.; Wang, Z. Q.; Jia, S.; Nakatsuji, S.; Amato, A.; Luetkens, H.; Xu, G.; Hasan, M. Z.; Guguchia, Z. Nodeless Kagome Superconductivity in $LaRu_3Si_2$. *Phys. Rev. Mater.* **2021**, *5*, No. 034803.
(7) Larsen, C. B.; Mazzone, D. G.; Gauthier, N.; Rosales, H. D.; Albarracín, F. A. G.; Lass, J.; Boraley, X.; Bud'ko, S. L.; Canfield, P. C.; Zaharko, O. Magnetic Ground State and Perturbations of the Distorted Kagome Ising Metal TmAgGe. *Phys. Rev. B* **2023**, *107*, No. 224419.
(8) Neupert, T.; Denner, M. M.; Yin, J.-X.; Thomale, R.; Hasan, M. Z. Charge Order and Superconductivity in Kagome Materials. *Nat. Phys.* **2022**, *18* (2), 137−143.
(9) Chamorro, J. R.; McQueen, T. M.; Tran, T. T. Chemistry of Quantum Spin Liquids. *Chem. Rev.* **2021**, *121* (5), 2898−2934.
(10) Wang, Y.; McCandless, G. T.; Wang, X.; Thanabalasingam, K.; Wu, H.; Bouwmeester, D.; Van Der Zant, H. S. J.; Ali, M. N.; Chan, J. Y. Electronic Properties and Phase Transition in the Kagome Metal $Yb_{0.5}Co_3Ge_3$. *Chem. Mater.* **2022**, *34* (16), 7337−7343.
(11) Meschke, V.; Gorai, P.; Stevanović, V.; Toberer, E. S. Search and Structural Featurization of Magnetically Frustrated Kagome Lattices. *Chem. Mater.* **2021**, *33* (12), 4373−4381.
(12) Jovanovic, M.; Schoop, L. M. Simple Chemical Rules for Predicting Band Structures of Kagome Materials. *J. Am. Chem. Soc.* **2022**, *144* (24), 10978−10991.
(13) Singh, H. K.; Sehrawat, A.; Shen, C.; Samathrakis, I.; Opahle, I.; Zhang, H.; Xie, R. High-Throughput Screening of Half-Antiperovskites with a Stacked Kagome Lattice. *Acta Mater.* **2023**, *242*, No. 118474.
(14) Mazin, I. I.; Jeschke, H. O.; Lechermann, F.; Lee, H.; Fink, M.; Thomale, R.; Valentí, R. Theoretical Prediction of a Strongly Correlated Dirac Metal. *Nat. Commun.* **2014**, *5*, No. 4261.
(15) Xiang, H. J.; Kan, E. J.; Wei, S. H.; Whangbo, M. H.; Gong, X. G. Predicting the Spin-Lattice Order of Frustrated Systems from First Principles. *Phys. Rev. B* **2011**, *84* (22), No. 224429.
(16) Hafner, J.; Wolverton, C.; Ceder, G. Toward Computational Materials Design: The Impact of Density Functional Theory on Materials Research. *MRS Bull.* **2006**, *31* (9), 659−668.
(17) Jha, D.; Choudhary, K.; Tavazza, F.; Liao, W. K.; Choudhary, A.; Campbell, C.; Agrawal, A. Enhancing Materials Property Prediction by Leveraging Computational and Experimental Data Using Deep Transfer Learning. *Nat. Commun.* **2019**, *10* (1), No. 5316.
(18) Kiely, E.; Zwane, R.; Fox, R.; Reilly, A. M.; Guerin, S. Density Functional Theory Predictions of the Mechanical Properties of Crystalline Materials. *CrystEngComm* **2021**, *23*, 5697−5710.
(19) Sparks, T. D.; Gaultois, M. W.; Oliynyk, A.; Brgoch, J.; Meredig, B. Data Mining Our Way to the next Generation of Thermoelectrics. *Scr. Mater.* **2016**, *111* (15), 10−15.
(20) Isayev, O.; Oses, C.; Toher, C.; Gossett, E.; Curtarolo, S.; Tropsha, A. Universal Fragment Descriptors for Predicting Properties of Inorganic Crystals. *Nat. Commun.* **2017**, *8*, No. 15679.
(21) Pilania, G.; Wang, C.; Jiang, X.; Rajasekaran, S.; Ramprasad, R. Accelerating Materials Property Predictions Using Machine Learning. *Sci. Rep.* **2013**, *3*, No. 2810.
(22) Choudhary, A. K.; Kini, A.; Hohs, D.; Jansche, A.; Bernthaler, T.; Csiszár, O.; Goll, D.; Schneider, G. Machine Learning-Based Curie Temperature Prediction for Magnetic 14:2:1 Phases. *AIP Adv* **2023**, *13* (3), No. 035112.
(23) Yong-Hong, Z.; Liu, B. G. First-Principles Study of Structural, Electronic, and Magnetic Properties of Mn_4XGe_3 (X = Fe, Co, Ni). *Chin. Phys. B* **2008**, *17* (9), 3417−3421.
(24) Aravindan, V.; Rajarajan, A. K.; Mahendran, M. First-Principles Study of Structural, Electronic, Magnetic and Elastic Properties of the Mn_2XSb (X = Co, Fe) Inverse Heusler Alloys. *J. Electron. Mater.* **2021**, *50* (4), 1786−1793.
(25) Saal, J. E.; Kirklin, S.; Aykol, M.; Meredig, B.; Wolverton, C. Materials Design and Discovery with High-Throughput Density Functional Theory: The Open Quantum Materials Database (OQMD). *JOM* **2013**, *65*, 1501−1509.
(26) Kirklin, S.; Saal, J. E.; Meredig, B.; Thompson, A.; Doak, J. W.; Aykol, M.; Rühl, S.; Wolverton, C. The Open Quantum Materials Database (OQMD): Assessing the Accuracy of DFT Formation Energies. *npj Comput. Mater.* **2015**, *1*, No. 15010.
(27) Jain, A.; Ong, S. P.; Hautier, G.; Chen, W.; Richards, W. D.; Dacek, S.; Cholia, S.; Gunter, D.; Skinner, D.; Ceder, G.; Persson, K. A. The Materials Project: A Materials Genome Approach to Accelerating Materials Innovation. *APL Mater.* **2013**, *1* (1), No. 011002.
(28) Singh, P.; Del Rose, T.; Palasyuk, A.; Mudryk, Y. Physics-Informed Machine-Learning Prediction of Curie Temperatures and Its Promise for Guiding the Discovery of Functional Magnetic Materials. *Chem. Mater.* **2023**, *35* (16), 6304−6312.
(29) Jiang, Y.; Jia, S.; Chen, S.; Li, X.; Wang, L.; Han, X. Theoretical Prediction and Experimental Validation of the Glass-Forming Ability and Magnetic Properties of Fe-Si-B Metallic Glasses from Atomic Structures. *Materials* **2022**, *15* (9), No. 3149.
(30) Sinha, M.; Vivanco, H. K.; Wan, C.; Siegler, M. A.; Stewart, V. J.; Pogue, E. A.; Pressley, L. A.; Berry, T.; Wang, Z.; Johnson, I.; Chen, M.; Tran, T. T.; Phelan, W. A.; McQueen, T. M. Twisting of 2D Kagomé Sheets in Layered Intermetallics. *ACS Cent. Sci.* **2021**, *7* (8), 1381−1390.
(31) Carter, E. A. Challenges in Modeling Materials Properties without Experimental Input. *Science* **2008**, *321* (5890), 800−803.
(32) Chamorro, J. R.; McQueen, T. M. Progress toward Solid State Synthesis by Design. *Acc. Chem. Res.* **2018**, *51* (11), 2918−2925.
(33) Welk, E.; Schuster, H.-U. Zur Kenntnis Der Phase $LiFe_6Ge_6$. *Z. Anorg. Allg. Chem.* **1976**, *424* (3), 193−197.
(34) Welk, E.; Schuster, H.-U. $LiFe_6Ge_5$ Und $LiFe_6Ge_4$ Zwei Phasen Mit Enger Strukturbeziehung Zu Der Verbindung $LiFe_6Ge_6/LiFe_6Ge_5$ and $LiFe_6Ge_4$ Two Phases with Close Structure Relations to the Compound $LiFe_6Ge_6$. *Z. Naturforsch. B* **1977**, *32* (7), 749−752.
(35) Cenzual, K.; Gelato, L. M.; Penzo, M.; Parthe, E. Overlooked Trigonal Symmetry in Structures Reported with Monoclinic Centred Bravais Lattices; Trigonal Description of Li_8Pb_3, PtTe, Pt_3Te_4, Pt_2Te_3, $LiFe_6Ge_4$, $LiFe_6Ge_5$, $CaGa_6Te_{10}$ and $La_{3.266}Mn_{1.1}S_6$. *Z. Kristallogr.-Cryst. Mater.* **1990**, *193* (3−4), 217−242.
(36) Givord, D.; Li, H. S.; de la Bâthie, R. P. Magnetic Properties of $Y2Fe_{14}B$ and $Nd_2Fe_{14}B$ Single Crystals. *Solid State Commun.* **1984**, *51* (11), 857−860.
(37) Sagawa, M.; Fujimura, S.; Togawa, N.; Yamamoto, H.; Matsuura, Y. New Material for Permanent Magnets on a Base of Nd and Fe (Invited). *J. Appl. Phys.* **1984**, *55* (6), 2083−2087.
(38) Ventrella, E. BS thesis. Investigating Itinerant Magnets for Magnetic Refrigeration 2017. http://purl.flvc.org/fsu/fd/FSU_libsubv1_scholarship_submission_1493404076.
(39) Canfield, P. C. New Materials Physics. *Rep. Prog. Phys.* **2020**, *83* (1), No. 016501.
(40) Adeyemi, A. N.; Bhaskar, G.; Cox, T.; Hong, S.; Gvozdetskyi, V.; Zaikina, J. V.Hydride Precursors in Materials Synthesis. In *Comprehensive Inorganic Chemistry III*, 3rd ed.; Elsevier, 2023; Vol. *1*−*10*, pp 128−146.
(41) Gvozdetskyi, V.; Sun, Y.; Zhao, X.; Bhaskar, G.; Carnahan, S. L.; Harmer, C. P.; Zhang, F.; Ribeiro, R. A.; Canfield, P. C.; Rossini, A. J.; Wang, C. Z.; Ho, K. M.; Zaikina, J. V. Lithium Nickel Borides: Evolution of [NiB] Layers Driven by Li Pressure. *Inorg. Chem. Front.* **2021**, *8* (7), 1675−1685.
(42) Mantravadi, A.; Gvozdetskyi, V.; Sarkar, A.; Mudryk, Y.; Zaikina, J. V. Exploring the A -V-Sb Landscape beyond AV_3Sb_5: A Case Study on the KV_6Sb_6 Kagome Compound. *Phys. Rev. Mater.* **2023**, *7* (11), No. 115002.
(43) Cox, T.; Gvozdetskyi, V.; Owens-Baird, B.; Zaikina, J. V. Rapid Phase Screening via Hydride Route: A Discovery of $K_{8-x}Zn_{18+3x}Sb_{16}$. *Chem. Mater.* **2018**, *30* (23), 8707−8715.
(44) Putz, H.; Brandenburg, K. *Match! - Phase Analysis using Powder Diffraction, Crystal Impact*, GbR, Kreuzherrenstr. 102, 53227 Bonn, Germany https://www.crystalimpact.de/match.

https://doi.org/10.1021/acs.inorgchem.4c03925
Inorg. Chem. 2024, 63, 24697−24708

(45) Toby, B. H.; Von Dreele, R. B. GSAS-II: The Genesis of a Modern Open-Source All Purpose Crystallography Software Package. *J. Appl. Crystallogr.* **2013**, *46* (2), 544−549.
(46) Chupas, P. J.; Chapman, K. W.; Kurtz, C.; Hanson, J. C.; Lee, P. L.; Grey, C. P. A Versatile Sample-Environment Cell for Non-Ambient X-Ray Scattering Experiments. *J. Appl. Crystallogr.* **2008**, *41* (4), 822−824.
(47) Klencsár, Z. *MossWinn 4.0i Manual*; Mosswinn, 2023.
(48) Sangster, J.; Pelton, A. D. The Ge-Li (Germanium-Lithium) System. *J. Phase Equilib.* **1997**, *18*, 289−294.
(49) Zeilinger, M.; Fässler, T. F. Structural and Thermodynamic Similarities of Phases in the Li−Tt (Tt = Si, Ge) Systems: Redetermination of the Lithium-Rich Side of the Li−Ge Phase Diagram and Crystal Structures of $Li_{17}Si_{4.0-x}Ge_x$ for x = 2.3, 3.1, 3.5, and 4 as Well as $Li_{4.1}Ge$. *Dalton Trans.* **2014**, *43*, 14959−14970.
(50) Teng, X.; Oh, J. S.; Tan, H.; Chen, L.; Huang, J.; Gao, B.; Yin, J. X.; Chu, J. H.; Hashimoto, M.; Lu, D.; Jozwiak, C.; Bostwick, A.; Rotenberg, E.; Granroth, G. E.; Yan, B.; Birgeneau, R. J.; Dai, P.; Yi, M. Magnetism and Charge Density Wave Order in Kagome FeGe. *Nat. Phys.* **2023**, *19* (6), 814−822.
(51) Avila, M. A.; Takabatake, T.; Takahashi, Y.; Bud'ko, S. L.; Canfield, P. C. Direct Observation of Fe Spin Reorientation in Single-Crystalline $YbFe_6Ge_6$. *J. Phys.: Condens. Matter.* **2005**, *17* (43), No. 6969.
(52) Mazet, T.; Malaman, B. Macroscopic Magnetic Properties of the $HfFe_6Ge_6$-Type RFe_6X_6 (X = Ge or Sn) Compounds Involving a Non-Magnetic R Metal. *J. Alloys Compd.* **2001**, *325* (1−2), 67−72.
(53) Venturini, G.; Welter, R.; Malaman, B. Crystallographic Data and Magnetic Properties of RT_6Ge_6 Compounds (R = Sc, Y, Nd, Sm, Gd, Lu; T = Mn, Fe). *J. Alloys Compd.* **1992**, *185* (1), 99−107.
(54) Hori, T.; Nishihara, R.; Akimitsu, M.; Ohoyama, K.; Onodera, H.; Yamaguchi, Y.; Mitsudo, S.; Motokawa, M. Magnetic Properties of hp13 Type TFe_6Ge_6(T = Zr, Nb, Hf) Alloys. *J. Magn. Magn. Mater.* **2001**, *226−230*, 1076−1078.
(55) Mazet, T.; Isnard, O.; Malaman, B. Neutron Diffraction and ^{57}Fe Mössbauer Study of the $HfFe_6Ge_6$-Type RFe_6Ge_6 Compounds (R = Sc, Ti, Zr, Hf, Nb). *Solid State Commun.* **2000**, *114* (2), 91−96.
(56) Schobinger-Papamantellos, P.; Buschow, K. H. J.; De Boer, F. R.; Ritter, C.; Isnard, O.; Fauth, F. The Fe Ordering in RFe_6Ge_6 Compounds with Non-Magnetic R (R = Y, Lu, Hf) Studied by Neutron Diffraction and Magnetic Measurements. *J. Alloys Compd.* **1998**, *267* (1−2), 59−65.
(57) Cadogan, J. M.; Ryan, D. H. Independent Magnetic Ordering of the Rare-Earth (R) and Fe Sublattices in the RFe_6Ge_6 and RFe_6Sn_6 Series. *J. Alloys Compd.* **2001**, *326* (1−2), 166−173.
(58) Dubiel, S. M. Relationship between the Magnetic Hyperfine Field and the Magnetic Moment. *J. Alloys Compd.* **2009**, *488* (1), 18−22.
(59) Mazet, T.; Ban, V.; Sibille, R.; Capelli, S.; Malaman, B. Magnetic Properties of $MgFe_6Ge_6$. *Solid State Commun.* **2013**, *159*, 79−83.
(60) Chevalier, B.; Bobet, J. L.; Pasturel, M.; Bauer, E.; Weill, F.; Decourt, R.; Etourneau, J. Ferromagnetic Behavior of the New Hydride $CeNiSnH_{1.8(2)}$. *Chem. Mater.* **2003**, *15* (11), 2181−2185.
(61) Gaudin, E.; Matar, S. F.; Pöttgen, R.; Eul, M.; Chevalier, B. Drastic Change of the Ferromagnetic Properties of the Ternary Germanide GdTiGe through Hydrogen Insertion. *Inorg. Chem.* **2011**, *50* (21), 11046−11054.
(62) Del Rose, T.; Choudhary, R.; Mudryk, Y.; Haskel, D.; Pathak, A. K.; Bhaskar, G.; Zaikina, J. V.; Johnson, D. D.; Pecharsky, V. K. Interplay between Kondo and Magnetic Interactions in $Pr_{0.75}Gd_{0.25}ScGeH$. *J. Alloys Compd.* **2023**, *966*, No. 171351.
(63) Yartys, V. A.; Denys, R. V.; Akselrud, L. G.; Vajeeston, P.; Dankelman, R.; Plomp, J.; Block, T.; Pöttgen, R.; Wragg, D.; Eggert, B. G. F.; Berezovets, V. Structure and Bonding in TiNiSi Type LaMgSnH Intermetallic Hydride. *J. Alloys Compd.* **2024**, *976*, No. 173198.
(64) Buxbaum, R. E.; Kinney, A. B. Hydrogen Transport through Tubular Membranes of Palladium-Coated Tantalum and Niobium. *Ind. Eng. Chem. Res.* **1996**, *35* (2), 530−537.

https://doi.org/10.1021/acs.inorgchem.4c03925
Inorg. Chem. 2024, 63, 24697−24708